Discover Mechanical Engineering

Research

Phase-field based shape optimization of uni- and multiaxially loaded nature-inspired porous structures while maintaining characteristic properties

Michael Selzer[1,4] · Leonie Wallat[1,3] · Nils Kersch[2] · Martin Reder[1,3] · Marcus Seiler[5] · Frank Poehler[2] · Britta Nestler[1,3,4]

Received: 21 June 2024 / Accepted: 18 September 2024
Published online: 14 November 2024

Abstract
Triply periodic minimal surfaces (TPMS) are highly versatile porous formations that can be defined by formulas. Computationally based, load-specific shape optimization enables tailoring these structures for their respective application areas and thereby enhance their potential. In this investigation, individual sheet-based gyroid structures with varying porosities are specifically optimized with respect to their stiffness. A modified phase-field method is employed to establish a simulation framework for the shape optimization process. Despite constant volume and the preservation of the periodicity of the unit cells, volume redistribution occurs through displacement of the interfaces. The phase-field-based optimization process is detailed using unidirectional loading on three gyroidal unit cells with porosities of 75 %, 80 %, and 85 %. Subsequently, the gyroidal unit cell with a porosity of 85 % is shape-optimized under multidirectional loading. A subsequent experimental validation of the unidirectionally loaded cells confirms that the shape-optimized structures exhibit, on average, higher stiffness than the non-optimized structures. The highest increase of 40 % in effective modulus is achieved with the gyroid structure having a porosity of 75 %, while maintaining minimal alteration to the surface-to-volume ratio and preserving periodicity. Additionally, the experimental data show that the optimization process resulted in a shift in the linear elasticity and plasticity range. In summary, the phase-field method proves to be a valid optimization technique for complex porous structures, allowing the preservation of characteristic properties.

Keywords Shape optimization · Gyroid · TPMS-structures · Phase-field

1 Introduction

Nature-inspired structures have been used for decades to develop new materials and designs with improved properties [1, 2]. A well-known example is the honeycomb structure inspired by the honeycomb of bees, which finds applications in various fields, from architecture to mechanical engineering [3]. Nowadays, additive manufacturing techniques such as electron beam melting [4], fused deposition modeling [5], or stereolithography [6] enable the

✉ Michael Selzer, michael.selzer@kit.edu; ✉ Leonie Wallat, leonie.wallat@partner.kit.edu | [1]Institute of Digital Materials Science, Karlsruhe University of Applied Sciences, Moltkestraße 30, Karlsruhe 76133, Baden-Wuerttemberg, Germany. [2]Institute of Materials and Processes, Karlsruhe University of Applied Sciences, Moltkestraße 30, Karlsruhe 76133, Baden-Wuerttemberg, Germany. [3]Institute for Applied Materials - Microstructure Modelling and Simulation, Karlsruhe Institute of Technology (KIT), Strasse am Forum 7, Karlsruhe 76131, Baden-Wuerttemberg, Germany. [4]Institute of Nanotechnology, Karlsruhe Institute of Technology (KIT), Hermann-von-Helmholtz-Platz 1, Eggenstein-Leopoldshafe 76344, Baden-Wuerttemberg, Germany. [5]ReOss GmbH, Echterdinger Str. 57, Filderstadt 70794, Baden-Wuerttemberg, Germany.

fabrication of complex structures and design possibilities [7]. This is particularly interesting for lightweight construction, as these structures are attractive due to their low weight and good mechanical properties. According to [8], the properties of cellular structures are determined by their material, relative density, and structure geometry. When considering cellular structures, a distinction is also made between whether the cell grids are periodic or stochastic [9].

Based on this, various types of cellular materials and corresponding methods and approaches for generating cellular structures exist in the literature. Stochastic cellular material can be generated using techniques like Voronoi tesselation [10] or interface-based methods [11].

A well-known example of periodic structures are triply periodic minimal surfaces (TPMS structures). These are naturally occurring structures that can be approximated by mathematical equations which parameterize their surface (see section 2). Characteristic features of these structures are that they have a smooth surface, and the unit cells of TPMS structures are periodic in every spatial direction. TPMS structures can further be distinguished between strut-based and sheet-based structure [12].

The present work focuses on sheet-based TPMS-structures characterized by a two-tunnel system, resulting in a high surface area to volume ratio (S/V ratio).

This makes these structures attractive for various applications and research areas. In the medical field, for example, a high S/V ratio in porous structures promotes cell growth [13], and it has been shown in [14] that the S/V ratio results in a higher oxygen transfer rate in a TPMS-based membrane design for blood gas transfer. In addition to the medical field, there are applications in other areas where a high S/V volume ratio is advantageous, such as in heat transfer, which is why TPMS structures are also considered as heat exchangers [15, 16].

Due to the promising and diverse applications of TPMS structures, various methods of structural optimization approaches are presented in the literature in order to further enhance specific material properties. The optimization is usually divided into three categories: size, shape, and topology [17].

Shape optimization alters the geometry of the structure, whereas its topological characteristics remain unchanged. In contrast, topology optimization does also consider topological changes of the structure [18]. Thus the resulting structure for topology optimization is independent of the initial structure, which is not the case for shape optimization [19].

However, some methods employed for topology optimization can also be used for shape optimization if the algorithm is stopped when topological changes start.

Different properties of the material can be subjected to optimization approaches aiming e.g. at increasing the effective stiffness [20]. The present work focuses on improving elastic properties of TPMS-structures. Various approaches to structural optimization can be found in literature ranging from manual adjustments in the parameterization of the geometry [21–25] to geometry-independent optimization approaches based on numerical full-field simulations [26, 27]. A commonly used adjustment of geometry parameterization is to introduce different kinds of porosity gradients into the cell structure [21–25]. As shown in different studies, the introduction of porosity gradients in gyroid TPMS-structures leads to an increase in stiffness under certain boundary conditions [24, 25] or help to improve the adaptability to natural bone environment in medical applications [22, 23]. In addition, different shape optimization methods based on numerical simulations exist in the field of structure mechanics. This includes the density-based solid isotropic material with penalization (SIMP) approach [28], which is employed by Guenther et al. [26] on TPMS structures. In this study, $3 \times 3 \times 3$ TPMS-cells (gyroid lattice and I-WP lattice) with a volume fraction of 25 % are considered for application in the field of tissue engineering. Another class of optimization approaches is based on the phase-field method. A significant advantage of the phase-field method lies in its ability to accommodate complex geometrical changes without adapting the numerical discretization [29].

This enables the generation of organic and natural forms that can better meet functional requirements than conventional designs [30].

Different models for phase-field based shape optimization are found in literature. Since the porosity of the structure should stay unchanged during optimization, volume preserving phase-field evolution equations need to be employed.

While using the fourth-order Cahn-Hilliard equation comes with relatively large computational cost, volume preserving Allen-Cahn approaches are only based on a second-order equation and thus save computational cost [31].

Allen-Cahn approaches have been employed for optimising different material properties in [32–34]. They predominantly focus on 2D structures, with few considering 3D structures [33].

Such approaches are also employed for mechanical topology optimization, where typically a loaded beam is analyzed, which eventually converges to a Michell-like structure [32, 34].

In the works of Takezawa [30, 35], a hollow tetrahedral cell structure is optimized using the Allen-Cahn approach aiming to design a cell structure with an isotropic stiffness while simultaneously improving manufacturability by electron beam melting.

This results in a TPMS-like material similar to Schwarz P structures [35]. While this study aims for an isotropic stiffness of a cell, the current work aims to optimize a cell according to the specific loading conditions.

In [27], three different gyroid TPMS-structures are shape-optimized under unidirectional predefined compressive loading using the Allen-Cahn approach. Subsequent experimental investigations of the optimized structures confirmed a correlation between the simulation-based and experimental results [36]. Furthermore, it is shown from the experimental data that optimization also leads to improvements of the plastic behaviour of the structures regarding their energy absorption capability. However, the shape-optimized structures from [27] lost their periodicity in all spatial directions. In contrast, the present work aims at preserving the periodicity.

Additionally, besides a unidirectional load case, the present work considers also multidirectional load scenarios.

In this work, sheet-based gyroid structures are shape-optimized using a phase-field method based on the Allen-Cahn approach. Several optimized structures are experimentally compared to the initial gyroid structures. The optimization aims to increase the effective stiffness under boundary conditions prescribing a specific macroscopic strain. Thereby characteristic properties of the structures, such as periodicity, are intended to be preserved throughout the optimization process. In contrast to most existing works, only a unit cell is considered here, as the periodicity is maintained in all spatial directions. Maintaining the periodicity of the cell allows the structure to be replicated in the respective spatial directions, resulting in design flexibility. Another advantage is the reduction in computational time compared to a multi-cell optimization process.

While in [27] a similar phase-field approach is used to optimize TPMS-structures, the homogeneous stress boundary conditions employed therein lead to a loss of periodicity of the optimized structure.

The present work is structured as follows. Chapter 2 addresses the generation of gyroid structures used as starting point for the optimization. The Phase-field based optimization method employed in this work is given in chapter 3. In order to enable an adequate comparison between the initial structure and the shape-optimized structures, the solid volume is being kept constant during the simulation. The optimization is applied on gyroid structures exhibiting three different volume fractions under uniaxial load. Furthermore, to demonstrate the applicability of this method in real-world scenarios, the sheet-based gyroid structure with a volume fractions of 15 % is optimized for three different cases of multiaxial loading. In addition to the effective modulus of elasticity, the change in surface area of the shape-optimized structure is examined. Finally, the optimization results for the uniaxial loading are validated by a comparison with experiments, where 3D-printed specimens of the initial and the optimized structures are used.

2 Structure generation

The structures are generated according to the algorithm presented in [27], which is implemented within the Pace3D framework. The structure generation and simulations were conducted using Pace3D, with the subsequent visualization performed using the open-source software ParaView. For this study, single-cell sheet-based gyroid structures with uniform porosities of 75 %, 80 %, and 85 % are fabricated and employed. The structurally defining parameter, porosity ρ, is defined as 1 minus the ratio of the volume V_{solid} of the solid material to the total volume V of the porous structure [37] yielding

$$\rho = 1 - \frac{V_{\text{solid}}}{V}. \tag{1}$$

Therefore, the gyroid structure with a porosity of 75 % has a volume fraction of 25 %, which corresponds to a dimensionless designation of V^*=0.25 [-]. In the following, the dimensionless designation V^* will be used for the volume fraction. The surfaces of gyroid structures are parametrized by the implicit equation

$$\begin{aligned} 0 = \Big[&\sin\left(2\pi\frac{x}{L_x}\right)\cos\left(2\pi\frac{y}{L_y}\right) + \sin\left(2\pi\frac{y}{L_y}\right)\cos\left(2\pi\frac{z}{L_z}\right) \\ &+ \cos\left(2\pi\frac{x}{L_x}\right)\sin\left(2\pi\frac{z}{L_z}\right)\Big]^2 - \delta^2. \end{aligned} \tag{2}$$

Hereby the design freedom of the gyroid structure is illustrated as representative for the other TPMS structures. According to the equation 2, the structures can be adjusted by various function parameters, such as cell size, cell repetitions, or porosity [38].

The cell structure is characterized by the number of cell repetitions in the *x*-, *y*-, and *z*-directions, as well as by the size of the unit cells L_x, L_y, L_z. The parameter δ controls the wall thickness and thus the porosity or solid volume fraction of the structure [39].

Figure 1 illustrates the sheet-based gyroid structure with three different volume fractions (V^*) of 0.25 [-], 0.2 [-], and 0.15 [-], which will be the focus of this paper.

3 Mathematical formulation

The subsequent section addresses the model used for computational shape optimization. To this end, effective material properties are defined and boundary conditions for the elastic problem are specified. An optimization approach based on a modified phase-field method is employed.

3.1 Effective elastic properties and boundary conditions

3.1.1 Homogenization of full-field simulations

The optimization procedure employed in this work is based on full-field simulations regarding elasticity. To obtain the macroscopic elastic behavior of a structure under a specific loading, a homogenization method is required to determine effective properties using the field information of a simulation. Thereby a single unit cell with volume $V = L_x L_y L_z$ is consider and Ω denotes the corresponding computational domain. Furthermore, $\boldsymbol{\epsilon}$ and $\boldsymbol{\sigma}$ denote the infinitesimal strain tensor and the Cauchy stress tensor, respectively. The strain tensor is defined as the symmetric gradient of the displacement field $\boldsymbol{u}$. A linear elastic material in a small deformation framework is considered yielding the constitutive equation

$$\boldsymbol{\sigma} = \mathbb{C}[\boldsymbol{\epsilon}] \tag{3}$$

with $\mathbb{C}$ being the fourth order stiffness tensor. The present work assumes that the Hill condition [40] holds, which is ensured by the boundary conditions employed. Therefore, the effective strain $\bar{\boldsymbol{\epsilon}}$ and the effective stress $\bar{\boldsymbol{\sigma}}$ can be determined by a volume average of the respective field yielding

$$\bar{\boldsymbol{\epsilon}} = \frac{1}{V}\int_\Omega \boldsymbol{\epsilon}\, \mathrm{d}V \quad \text{and} \quad \bar{\boldsymbol{\sigma}} = \frac{1}{V}\int_\Omega \boldsymbol{\sigma}\, \mathrm{d}V. \tag{4}$$

Defining the effective stiffness $\bar{\mathbb{C}}$ and compliance $\bar{\mathbb{S}} = \bar{\mathbb{C}}^{-1}$ tensors, the effective constitutive equations for an elastic material are given by

$$\bar{\boldsymbol{\sigma}} = \bar{\mathbb{C}}[\bar{\boldsymbol{\epsilon}}] \quad \text{and} \quad \bar{\boldsymbol{\epsilon}} = \bar{\mathbb{S}}[\bar{\boldsymbol{\sigma}}]. \tag{5}$$

The Hill condition implies energetic equivalence of the effective quantities with the actual field quantities. Therefore, the average elastic strain energy density $\bar{f}_{\mathrm{el}}$ and the complementary energy density $\bar{f}^*_{\mathrm{el}}$ are obtained via

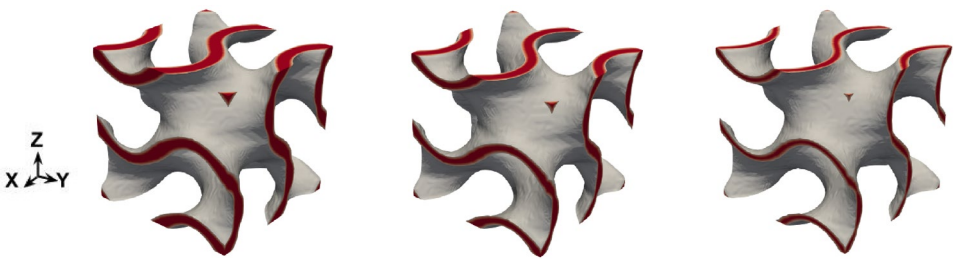

(a) $V^* = 0.25\,[-]$ (b) $V^* = 0.2\,[-]$ (c) $V^* = 0.15\,[-]$

Fig. 1 Sheet-based gyroid structures with volume fractions V^* of **a** 0.25 [-], **b** 0.2 [-], and **c** 0.15 [-]

$$\bar{f}_{\mathrm{el}} = \frac{1}{2V}\int_{\Omega} \boldsymbol{\epsilon}\cdot\mathbb{C}[\boldsymbol{\epsilon}]\,\mathrm{d}V = \frac{1}{2}\bar{\boldsymbol{\epsilon}}\cdot\bar{\mathbb{C}}[\bar{\boldsymbol{\epsilon}}] \quad \text{and}$$
$$\bar{f}^{*}_{\mathrm{el}} = \frac{1}{2V}\int_{\Omega} \boldsymbol{\sigma}\cdot\mathbb{S}[\boldsymbol{\sigma}]\,\mathrm{d}V = \frac{1}{2}\bar{\boldsymbol{\sigma}}\cdot\bar{\mathbb{S}}[\bar{\boldsymbol{\sigma}}], \tag{6}$$

respectively. The $[\cdot]$ denotes the linear mapping of second-order tensors. Note, that equivalence between elastic strain energy and complementary energy holds, and thus $\bar{f}_{\mathrm{el}} = \bar{f}^{*}_{\mathrm{el}}$. Given, that $\boldsymbol{\sigma}$ and $\boldsymbol{\epsilon}$ are known from full-field simulations, $\bar{\boldsymbol{\sigma}}$ and $\bar{\boldsymbol{\epsilon}}$ are obtained by equation (4).

With these, the effective Young's modulus in the present work is determined following the approach from [41].

3.1.2 Objective function

The aim of the present optimization is to increase the effective stiffness and, in consequence, reduce the effective compliance under a given load case. If the effective stress $\bar{\boldsymbol{\sigma}}$ is prescribed by stress boundary conditions, as it is the case in [27], a reduction of the effective compliance is equivalent to a minimization of the strain energy due to $\bar{f}_{\mathrm{el}} = \bar{f}^{*}_{\mathrm{el}} = \frac{1}{2}\bar{\boldsymbol{\sigma}}\cdot\bar{\mathbb{S}}[\bar{\boldsymbol{\sigma}}]$. Increasing the effective stiffness is therefore equivalent to a minimization of the strain energy and thus $\min(\bar{f}_{\mathrm{el}})$ under constant $\bar{\boldsymbol{\sigma}}$. Conversely, if the effective strain $\bar{\boldsymbol{\epsilon}}$ is prescribed by application of displacement boundary conditions, an increase of effective stiffness is achieved by maximizing the strain energy because $\bar{f}_{\mathrm{el}} = \frac{1}{2}\bar{\boldsymbol{\epsilon}}\cdot\bar{\mathbb{C}}[\bar{\boldsymbol{\epsilon}}]$. In this case, the optimization problem $\max(\bar{f}_{\mathrm{el}})$ under constant $\bar{\boldsymbol{\epsilon}}$ reproduces the desired behaviour. Therefore, different objective functions for setups with different mechanical boundary conditions need to be considered.

3.1.3 Boundary condition

The present work employs boundary conditions specifying $\bar{\boldsymbol{\epsilon}}$ and therefore, the strain energy density should be maximized. To satisfy both the specification of an effective strain and periodicity in all spatial directions the fluctuation $\widetilde{\boldsymbol{u}}(\boldsymbol{x}) = \boldsymbol{u}(\boldsymbol{x}) - \bar{\boldsymbol{\epsilon}}\boldsymbol{x}$ of the displacement field $\boldsymbol{u}$ at a spatial point $\boldsymbol{x}$ is defined. Regarding the displacement fluctuations periodicity is enforced using $\widetilde{\boldsymbol{u}}_{\mathrm{upper}} = \widetilde{\boldsymbol{u}}_{\mathrm{lower}}$. Hereby, $\widetilde{\boldsymbol{u}}_{\mathrm{upper}}$ and $\widetilde{\boldsymbol{u}}_{\mathrm{lower}}$ are the values at the lower and upper boundary in one direction, e.g. regarding the x-direction $\widetilde{\boldsymbol{u}}_{\mathrm{upper}} = \widetilde{\boldsymbol{u}}(L_x, y, z)$ and $\widetilde{\boldsymbol{u}}_{\mathrm{lower}} = \widetilde{\boldsymbol{u}}(0, y, z)$ hold. In consequence, the present work employs the displacement boundaries

$$\boldsymbol{u}(L_x, y, z) = \boldsymbol{u}(0, y, z) + L_x\bar{\boldsymbol{\epsilon}}\boldsymbol{e}_x, \tag{7a}$$

$$\boldsymbol{u}(x, L_y, z) = \boldsymbol{u}(x, 0, z) + L_y\bar{\boldsymbol{\epsilon}}\boldsymbol{e}_y, \tag{7b}$$

$$\boldsymbol{u}(x, y, L_z) = \boldsymbol{u}(x, y, 0) + L_z\bar{\boldsymbol{\epsilon}}\boldsymbol{e}_z, \tag{7c}$$

where $\boldsymbol{e}$ denotes the unit vector in the respective coordinate direction. Thereby, both an effective strain is prescribed while still retaining periodicity.

3.2 Optimization using a modified phase-field method

3.2.1 Phase-field method

The structural optimization is based on the phase-field method, which is a proven tool for problems such as phase transformations [42, 43] or structural mechanics in multigrain systems [44, 45] as well as porous structures [41]. For a problem with N phases, the geometry is described by the tuple $\boldsymbol{\phi} = \{\phi_1, \ldots, \phi_N\}$ of phase variables $\phi_\alpha(\boldsymbol{x}, t)$. These phase variables indicate whether phase α is present at a point $\boldsymbol{x}$ or not, corresponding to values of 1 or 0. Instead of a sharp dividing surface between different phases, a smooth transition region is employed, resulting in a diffuse interface with finite thickness, where ϕ_α exhibits values between 0 and 1. Therefore, the phase variable ϕ_α can be regarded as the local volume fraction of phase α. This allows for the application of interpolation techniques at the diffuse interface, avoiding the need for body-fitted meshes in the numerical solution process [46]. The evolution of the phase-field is typically derived from a minimization of a Ginzburg-Landau free energy density functional which depends on the phase-field

tuple and the corresponding gradients [47]. Typically, the free energy functional $\mathcal{F}(\boldsymbol{\phi}, \nabla\boldsymbol{\phi}) = \mathcal{F}_{\text{int}}(\boldsymbol{\phi}, \nabla\boldsymbol{\phi}) + \mathcal{F}_{\text{bulk}}(\boldsymbol{\phi}, \dots)$ is additively split into an interfacial contribution $\mathcal{F}_{\text{int}}$ and a contribution of the bulk regions $\mathcal{F}_{\text{bulk}}$ [48, eq. (1)]. The latter contribution may arise from the mechanical strain energy cf. [49]. If the elastic energy is the only bulk contribution, like it is the case for the present work, it is written as

$$\mathcal{F}_{\text{bulk}} = \mathcal{F}_{\text{el}}(\boldsymbol{\phi}, \boldsymbol{u}) = \int_{\Omega} f_{\text{el}} \, \mathrm{d}V = V\bar{f}_{\text{el}} \tag{8}$$

making use of equation (6). The interfacial contribution is expressed as

$$\mathcal{F}_{\text{int}}(\boldsymbol{\phi}, \boldsymbol{u}) = \int_{\Omega} f_{\text{grad}}(\boldsymbol{\phi}, \nabla\boldsymbol{\phi}) + f_{\text{pot}}(\boldsymbol{\phi}) \, \mathrm{d}V \tag{9}$$

comprising a gradient energy density f_{grad} and a potential energy f_{pot}. The free energy minimization requires the variation of $\mathcal{F}$ to vanish, thus $\delta\mathcal{F} = 0$. Variational calculus can be used to obtained governing equations for all occurring solution variables. Regarding mechanics, this gives rise to the momentum balance. With respect to the phase-field, an additional ansatz regarding the relaxation to equilibrium allows to obtain phase-field evolution equations. Thereby one way to derive evolution equations is to follow an Allen-Cahn approach [50] which can be formulated with a constraint of volume preservation of phases [51]. An Allen-Cahn type phase-field method is employed in the present work with some minor modifications in order to use it for optimizing structures by means of maximizing stiffness under a given load while preserving the phase volume.

3.2.2 Governing equations

The present work considers a two-phase problem with a solid phase (ϕ_{s}) and a porous phase (ϕ_{p}). Here, it is assumed that the porous phase exhibits no stiffness and accordingly stresses can arise in the solid phase only. Therefore, using the ansatz of Khachaturian [52], the interpolated strain energy density reads

$$f_{\text{el}} = \frac{1}{2} h(\phi_{\text{s}}) \boldsymbol{\epsilon} \cdot \mathbb{C}_{\text{s}}[\boldsymbol{\epsilon}] \tag{10}$$

with $\mathbb{C}_{\text{s}}$ being the stiffness of the solid phase and $h(\phi_{\text{s}})$ an interpolation function. In the further course of this work $h(\phi_{\text{s}}) = \phi_{\text{s}}$ is chosen, but also different choices are possible, cf., e.g. [53]. In order to maximise the stiffness, the objective function

$$\mathcal{F} = \int_{\Omega} f_{\text{el}} \, \mathrm{d}V = \int_{\Omega} \frac{1}{2} h(\phi_{\text{s}}) \mathbb{C}_{\text{s}}[\boldsymbol{\epsilon}] \cdot \boldsymbol{\epsilon} \, \mathrm{d}V \tag{11}$$

is used. The optimization problem considered in the present work is

$$\max\left(\mathcal{F}(\phi_{\text{s}})\right) \quad \text{under} \quad \int_{\Omega} \phi_{\text{s}} \, \mathrm{d}V = V_{\text{solid}}, \quad \frac{1}{V}\int_{\Omega} \boldsymbol{\epsilon} \, \mathrm{d}V = \bar{\boldsymbol{\epsilon}} \tag{12}$$

with V_{solid} being the solid volume and $\bar{\boldsymbol{\epsilon}}$ the effective strain prescribed by boundary conditions of the elastic problem. The design variable of the optimization problem is the phase-field ϕ_{s} of the solid phase, which defines the geometry of the structure. The given optimization problem differs from the classical phase-field approach in two points. Firstly, no interfacial contributions are included in the objective function. Secondly, due to the boundary conditions employed, the mechanical free energy should be maximized instead of minimizing it. The optimization given by equation (12) is achieved using the phase-field evolution equation yield by the volume preserving Allen-Cahn approach with an obstacle potential and a correction eliminating the curvature minimizing dynamics. Thus, the system of partial differential equations considered in this work contains the stationary momentum balance and the Allen-Cahn equation reading

$$\nabla \cdot (\boldsymbol{\sigma}) = 0, \tag{13}$$

$$\frac{\partial \phi_s}{\partial t} = \frac{M}{\epsilon}\left[2\gamma\epsilon(\Delta\phi_s - \|\nabla\phi_s\|\nabla\cdot\boldsymbol{n}) - \frac{16\gamma}{\pi^2\epsilon}(1-2\phi_s) - \lambda_{\text{vol}} + \frac{\partial h(\phi_s)}{\partial\phi_s} f_{\text{el}}\right], \tag{14}$$

with the stress $\boldsymbol{\sigma} = h(\phi_s)\mathbb{C}_s[\epsilon]$ and strain energy density $f_{\text{el}} = \frac{1}{2}\mathbb{C}_s[\epsilon]\cdot\epsilon$. Herein M is a mobility coefficient, γ the surface tension, and ϵ a parameter determining the width of the diffuse interface. The volume preservation is ensured by the Lagrange multiplier λ_{vol} cf. [51]. Furthermore, the term $\|\nabla\phi_s\|\nabla\cdot\boldsymbol{n}$ with $\boldsymbol{n} := \nabla\phi_s/\|\nabla\phi_s\|$ eliminates the curvature minimizing dynamics of the Allen-Cahn equation (14) [44, 54]. Therefore, the interface terms proportional to γ only lead to a relaxation to the phase-field equilibrium profile while preserving the actual geometry which can be identified with the iso-surface where $\phi_s = 0.5$. Thus, in context of the present work, the surface tension γ is not a physical parameter. Instead it represents a model parameter which needs to be chosen large enough in order to counteract deformations of the diffuse interface and preserve the phase-field equilibrium profile. The geometrical change during the shape optimization is caused by the driving force term including the elastic strain energy density f_{el}. It is noted, that in contrast to physical elasticity driven phase-transformation (cf., e.g. [44]), the sign of this driving force term is switched due to the formulation of the optimization problem aiming to maximize $\bar{f}_{\text{el}}$ due to the displacement boundary conditions.

3.2.3 Numerical discretization

To solve the differential equation system the software package Pace3D [55] is utilized which is a software framework for simulation of microstructure evolution based on the phase-field method. The spatial discretization implemented with an equidistant Cartesian grid. The phase-field evolution equation (14) is discretized through a finite-difference method with explicit time integration. In each time increment, the stationary momentum balance (13) is solved using a linear finite element discretization. Additional information regarding the discretization are given in appendix A. Further insights into the solution methodology are also delineated in [49], wherein an akin strategy is adopted for integrating elasticity and phase evolution.

The simulations carried out in the present work are based on a small deformation framework with a linear elastic constitutive law. Therefore, due to linearity, the findings are independent of the stiffness of the solid material. Following [41], the subsequent results are given in normalized manner. Thereby, the effective modulus is normalized by its solid material E_s.

3.2.4 Model parameters

Within this work, single-cell gyroid structures in a three-dimensional domain Ω are considered, each with 200 cells in each spatial direction. The shape optimization conducted in the subsequent course is carried out using $\epsilon = 0.015L$, which corresponds to an interface width of approximately $0.0375L$, considering the edge length $L = 1$ m of the domain. This choice ensures a resolution of the diffuse interface with a number of 7 cells. Furthermore, in the discretized version of equation (14), the mobility parameter $M = 1.0\text{m}^2\text{skg}^{-}1$and the timestep size $\Delta t = 1.75e-4s$ are chosen. The surface tension $\gamma = 0.02\text{kg s}^{-}2$ is used which for the given parameter set leads to preservation of the phase-field equilibrium profile.

3.2.5 Overview of the optimization procedure

For the optimization process, the Gyroid structure is adjusted so that the stiffness is increased under a specific load by shifting the boundary surfaces. The goal is to enhance the stiffness for the given load case. The process continues until the volume distribution results in a significant topological change. The simplified sequence of this process is illustrated in Fig. 2.

4 Results and discussion

In the following, gyroid unit cells with a volume fraction of 0.25 [-], 0.2 [-], and 0.15 [-] are shape optimized under loading with a predefined effective strain. This chapter is divided into two parts.

The first part addresses shape optimization of the structures under unidirectional and multidirectional load scenarios and provides a discussion on the corresponding simulation results.

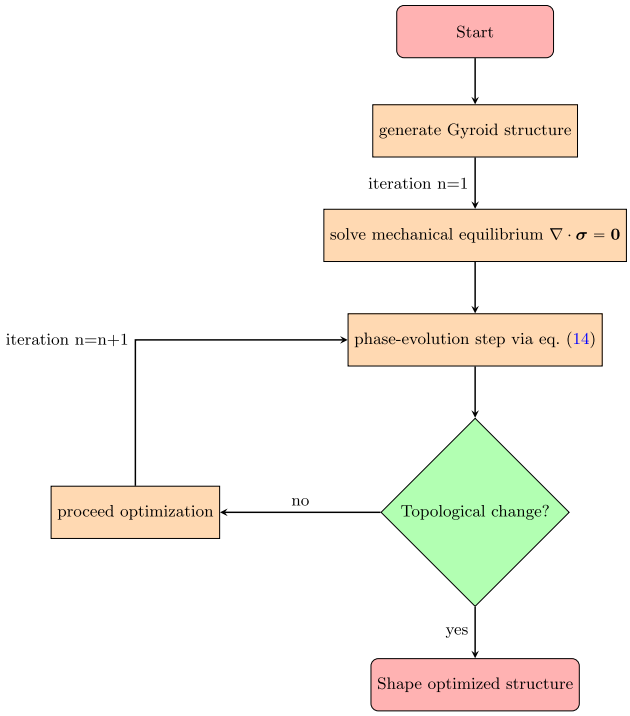

Fig. 2 Flow chart of the shape optimization process

The second part focuses on the experimental validation of the original and the optimized structures subjected to unidirectional loading. The results yield by simulations and experiments are compared.

4.1 Phase-field-based shape optimization

With the modified phase-field method described in subsection 3, gyroid unit cells are shape optimized. Initially, these cells are subjected to unidirectional loading, followed by optimization under multidirectional loading conditions.

4.1.1 Unidirectional loading

The structures resulting from the shape optimization for the respective volume fraction of 0.25 [-], 0.2 [-], and 0.15 [-] under a uniaxial load in *x*-direction can be found in Fig. 3.

According to the objective of shape optimization, the original form of the unit cell is preserved. Moreover, the periodicity of the unit cell is maintained, which allows for a later multiplication of the unit cells in the respective spatial directions. During the optimization process, among other things, the cross-braces in the *x*-direction have thinned, which is highlighted in the marked area.

To analyze the volume distribution through the optimization process in more detail, in the *x*-direction, the altered layer-wise volume fraction from the initial structure (solid green line) compared to the optimized structure (dotted grey line) is shown in Figs. 4, 5,6. Additionally, the solid red line shows the difference in volume fraction between the original structure and the optimized structure. In this context, the black zero line separates the areas where a positive difference

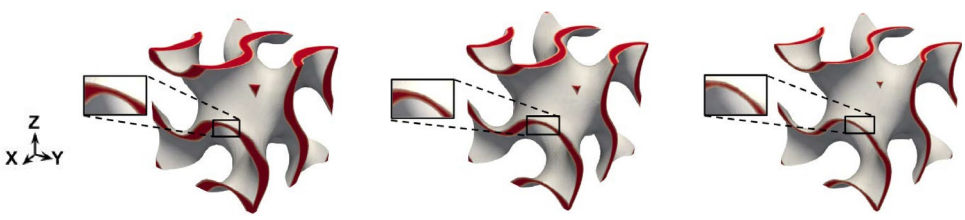

(a) $V^* = 0.25\,[-]$ (b) $V^* = 0.2\,[-]$ (c) $V^* = 0.15\,[-]$

Fig. 3 Shape-optimized sheet-based gyroid structures with volume fractions V^* of **a** 0.25 [-], **b** 0.2 [-], and **c** 0.15 [-]

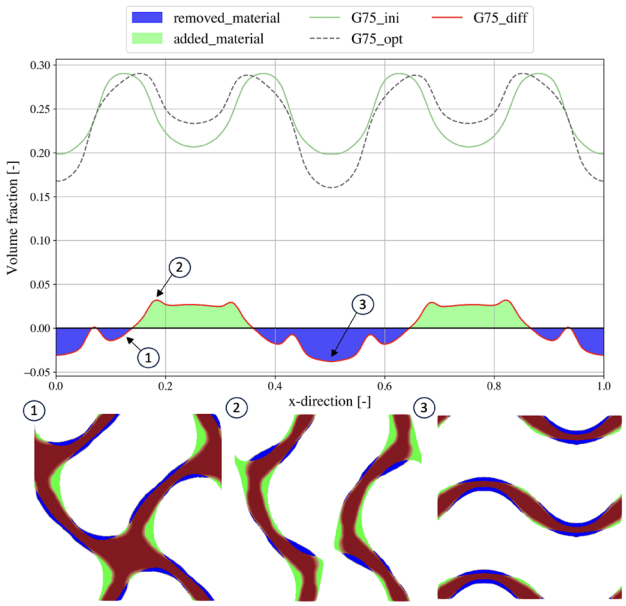

Fig. 4 Comparison of the plane-wise volume fraction (on the *yz*-axis) along the *x*-direction between the initial (G75_ini, solid line) and the optimized (G75_opt, dashed line) gyroid structure, illustrating the areas where material is added (light-green) and removed (blue) during the optimization process

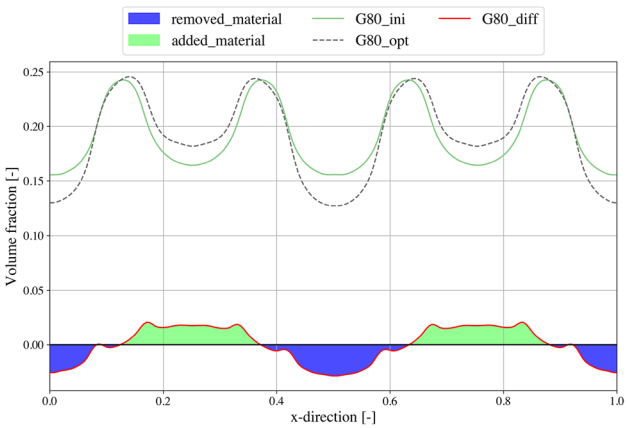

Fig. 5 Comparison of the plane-wise volume fraction (on the *y*-axis) along the *x*-direction between the initial (G80_ini, solid line) and the optimized (G80_opt, dashed line) gyroid structure, along with a representation of areas where material is added (green) or removed (blue) during the optimization process, depicted by the difference (red line)

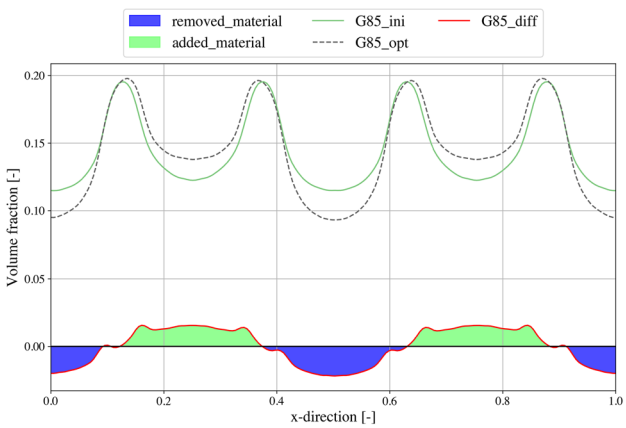

Fig. 6 Comparison of the plane-wise volume fraction (on the *y*-axis) along the *x*-direction between the initial (G85_ini, solid line) and the optimized (G85_opt, dashed line) gyroid structure, along with a representation of areas where material is added (green) or removed (blue) during the optimization process, depicted by the difference (red line)

is above and a negative difference is below the line. A positive difference indicates an increase in material addition, while a negative difference indicates a predominant removal of material. The blue-marked areas below the difference line indicate the planes where more material is removed compared to the original structure due to the displacement of the interfaces. The green-marked area above the difference line shows the planes where material is added. The *x*-direction represents the normalized coordinate *x*/*L*. When examining the difference curves of the structures, it becomes clear

Table 1 Structural and mechanical properties of the initial and shape-optimized gyroid-structure

Structure:	85%			80%			75%		
	V^*	Surface	$\bar{E}/E_s$ (dim.less)	V^*	Surface	$\bar{E}/E_s$ (dim.less)	V^*	Surface	$\bar{E}/E_s$ (dim.less)
Initial	0.243	5.976	275.390	0.192	6.027	0.064	0.144	6.044	0.087
Optimized	0.243	5.981	0.067	0.192	5.993	0.089	0.144	5.974	0.128

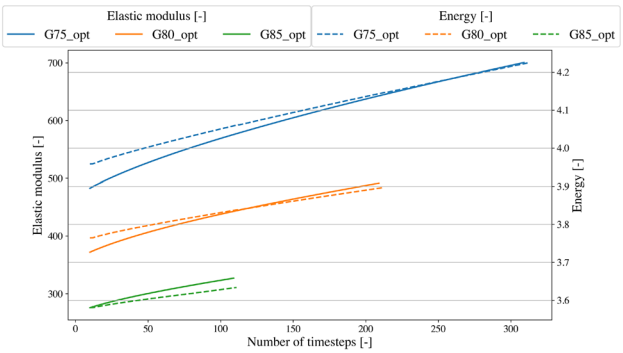

Fig. 7 Relationship between the energy evolution (dashed line) and the modulus of elasticity (solid line) across the simulation of the three considered gyroidal unit cells with a volume fraction of 0.25 [-] (G75_opt), 0.2 [-] (G80_opt), and 0.15 [-] (G85_opt)

that the material redistribution has taken place in the same areas for all three structures, and the difference curve has a periodic course. Comparing the three diagrams of the gyroidal unit cells with a volume fraction of 0.25 [-], 0.2 [-], and 0.15 [-] shows that the volume redistribution occurred in the same places. Due to the larger initial volume, a higher volume change is observed in the gyroid structure with a volume fraction of 0.25 [-]. Therefore, this structure is chosen to illustrate the volume redistribution based on three different planes, which are shown in Fig. 4 in connection with the difference. Since continuous shape optimization would lead to the complete removal of the webs, the simulation process is terminated at this point.

Cross-sectional image 1 of Fig. 4 corresponds to an area between the maximum and minimum difference. Here, it is evident that material is added at the branches and material is removed from the cross-braces.

The displayed layers of the extreme points from the Fig. 4 correspond to where a lot of material has been added or removed. The respective planes of the structure, where the global maximum and minimum of the changed volume fraction from the gyroid structure with a porosity of 75 % in comparison with the initial structure, is shown in cross-sectional images 2 and 3 in Fig. 4. In image 3, it is evident that the cross-braces in the non-loading direction are reduced. This observation can also be made in the marked areas of Fig. 3.

The previously presented load-specific changes lead to structural and mechanical property changes, which are listed in Table 1.

Generally, from the "Volume fraction" column, it is observable that the target volume fraction of 0.25 [-], 0.2 [-], and 0.15 [-] is not precisely achieved. The gyroid cell with a volume fraction of 0.2 [-] deviates from its target volume fraction by about 2 % the least, while the other two structures deviate by approximately 4 % from the set target volume fraction. Increasing the cell area, enhances the accuracy of the structuring, but requires significantly larger computation times for the simulation. Additionally, it is noticeable that structures with a higher volume fraction have a smaller surface area. Through the shape optimization process, the surface area decreases by about 1 % for the unit cell with a volume fraction of 0.2 [-] and 0.15 [-]. Only for the gyroid structure with a volume fraction of 0.15 [-] a slight increase in surface area is observed. Additionally, it is observable that an increase in the effective dimensionless Young's modulus is achieved through the interface displacement for all three structures. For the structure with a volume fraction of 0.25 [-], the highest increase in the Young's modulus of about 45 % is achieved. From the Fig. 7, the relationship between the increase in energy (dashed line) and the resulting increase in the effective Young's modulus (solid line) throughout the entire simulation process (number of time steps) is shown.

The modulus of elasticity is given in dimensionless form by $\bar{E}/E_s$, and similarly the dimensionless energy $\bar{f}_{el}/E_s$ is used. The transformation into dimensionless parameters enables material-independent statements, which is possible due to linearity. As already explained in Chapter 3, it is noticeable that the displacement of the interfaces results in an increase in energy, which simultaneously leads to an increase in stiffness. Accordingly, an increase in stiffness could be achieved for all three structures. Moreover, the diagram reveals that the energy and the Young's modulus have different slopes.

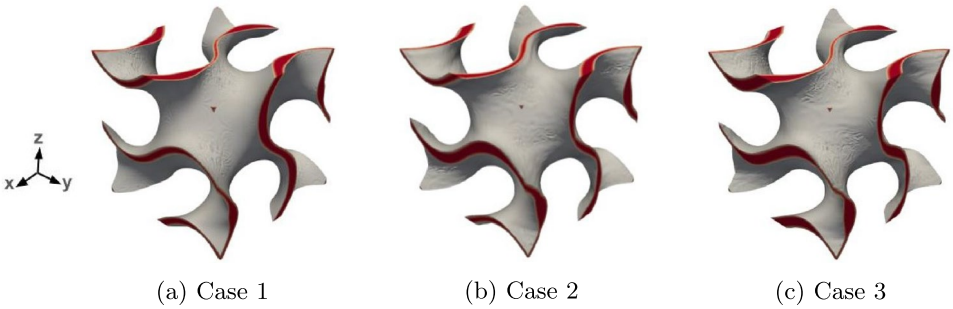

(a) Case 1 (b) Case 2 (c) Case 3

Fig. 8 Load-specific shape-optimized, sheet-based gyroid structures under multidirectional loading with a volume fraction of 0.15 [-], based on the load cases Case 1 to Case 3 as presented in equation 15

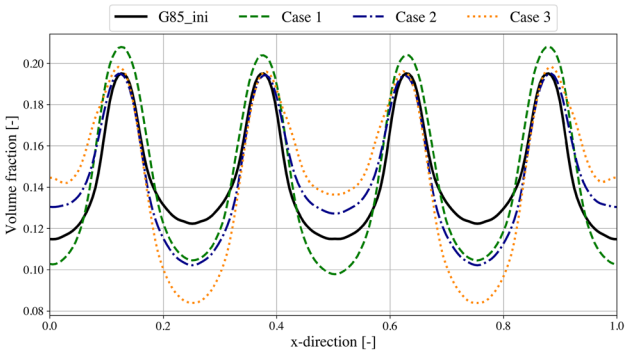

Fig. 9 Volume fraction distribution in the *x*-direction of the initial structure and the shape-optimized structures under multi-axial loading for three different cases: Case 1, Case 2 and Case 3

This can be attributed to the weighting during the simulation process. It is also striking that, depending on the different porosities, the structures under consideration are characterized by different numbers of iterations during the optimization process. Since the simulation is terminated just before a topology change occurs due to interface displacement, the largest amount of optimization iterations to reach this point occurs for the gyroid structure with a volume fraction of 0.25 [-] is the longest. As a result, the highest energy change and accordingly the highest increase in stiffness are achieved.

4.1.2 Multidirectional loading

In practical applications, multiple loading conditions in different spatial directions are often relevant [56]. In the following, gyroid unit cells with a volume fraction of 0.15 % are subjected to multidirectional loading and optimized for each loading case. Diverse optimization possibilities are illustrated using the phase-field method. Similar to the unidirectional case, the volume fraction is kept constant, resulting in volume redistribution during the simulation. To consider more complex loading scenarios, shear loading is prescribed in addition to uni-axial strain. As in previous simulations, the simulation is terminated once the topology changes. Three different combinations of loading cases are considered applying the macroscopic strain $\varepsilon = 0.01$ in different directions according to

$$\bar{\boldsymbol{\epsilon}}_{\text{case1}} = \begin{bmatrix} 0 & -\varepsilon & 0 \\ -\varepsilon & -\varepsilon & 0 \\ 0 & 0 & -\varepsilon \end{bmatrix}, \quad \bar{\boldsymbol{\epsilon}}_{\text{case2}} = \begin{bmatrix} 0 & -\varepsilon & 0 \\ -\varepsilon & -\varepsilon & -\varepsilon \\ 0 & -\varepsilon & 0 \end{bmatrix}, \quad \bar{\boldsymbol{\epsilon}}_{\text{case3}} = \begin{bmatrix} 0 & 0 & 0 \\ 0 & -\varepsilon & -\varepsilon \\ 0 & -\varepsilon & 0 \end{bmatrix}. \tag{15}$$

The respective shape-optimized structures corresponding to the load cases depicted in Formula 15 are shown in Fig. 8.

Similarly to the one-dimensional loading case, the topology is not disrupted during the shape optimization process under multidirectional loading. Fig. 9 illustrates the volume redistribution for the three considered cases along the *x*-direction.

The initial volume fraction distribution of the structure is included in the diagram as reference data (solid black line). The diagram reveals that the volume is redistributed differently depending on the loading case, resulting

Table 2 Structural and mechanical properties of the original and shape-optimized gyroid structure with a volume fraction of 0.15 [-] under multiaxial loading in the specified direction with a predetermined strain ϵ and shear τ of 1 %

Structure:	Case 1: *xy*-direction; *yy*-direction; *zz*-direction			Case 2: *xy*-direction; *yy*-direction; *yz*-direction			Case 3: *yy*-direction; *yz*-direction		
	V^*	Surface	$\bar{E}/E_s$ (dim.less)	V^*	Surface	$\bar{E}/E_s$ (dim.less)	V^*	Surface	$\bar{E}/E_s$ (dim.less)
Initial	0.144	6.045	0.051	0.144	6.045	0.051	0.144	6.045	0.051
Optimized	0.144	5.915	0.081	0.144	5.975	0.073	0.144	5.936	0.081

in load-specific volume fraction profiles with locally varying volume increases or decreases along the considered *x*-direction.

While the redistribution of volume led to an increase in the stiffness of the respective structures in the corresponding loading directions, the periodicity of the unit cell could simultaneously be maintained. Consequently, an increase in the effective modulus of elasticity is achieved in all three structures, as indicated in Table 2.

When comparing the effective modulus of the initial structures, it becomes evident that it lies within similar ranges for the three considered loading cases. The largest increases in the modulus of elasticity are achieved through optimization in loading cases 1 and 3. This is attributed to the need to terminate the simulation for case 2 prematurely to prevent a change in the structure's topology. While a percentage increase of the dimensionless effective modulus of elasticity of up to approximately 60 % (case 3) is achieved, there is a slight reduction in surface area of up to 2.1 %.These three examples illustrate that the phase-field method is a suitable approach for stress-specific optimization of complex porous structures under multidirectional loading, while maintaining the volume and periodicity during the optimization process.

4.2 Experimental validation

The main objective of the experimental validation is to confirm, that the computed candidates are indeed structurally optimized for the imposed mechanical loading treatments.

For the experimental validation, the unidirectionally shape-optimized gyroid structures are used. Herefore, the initial structures and the uni-dimensionally loaded, shape-optimized gyroid structures are manufactured using additive manufacturing and subsequently tested by applying mechanical loads.

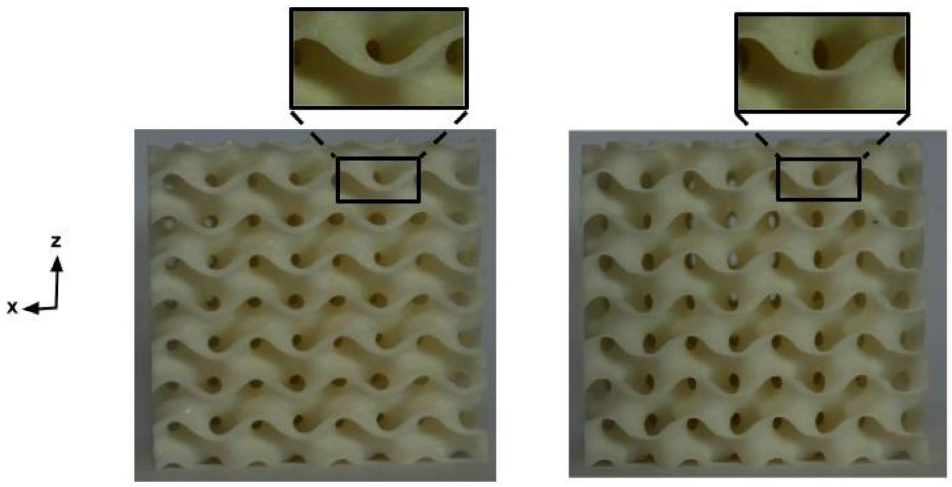

(a) Ini. structure: $V^* = 0.25\,[-]$ (b) Opt. structure: $V^* = 0.25\,[-]$

Fig. 10 *xz*-plane of the initial (a) and optimized (b) printed sheet-based gyroid structure with a volume fraction of $V^* = 0.25\,[-]$

4.2.1 Manufacture of structures

The original and optimized unit cells are replicated four times in each of the three dimensions (*x*, *y*, and *z*- direction) for experimental validation, resulting in a total size of 4*x*4*x*4 cells.. The specimen size of about 50.8 mm in each spatial direction meets the minimum requirements of the standard presented in subsection 4.2.2.

The test specimens are manufactured using Standard Photopolymer Resin (Elegoo Inc) in white color on the Stereolithography (SLA) 3D printer ELEGOO MARS 2. For slicing the structures, the software Chitubox Version 1.9.5 was used. Each test specimen is printed five times and subsequently tested. Figure 10 illustrates the initial and optimized gyroid structure with a volume fraction of 0.15 [-], serving as an exemplary case for the other test specimens.

The *xz*-plane of the printed test specimens is shown to illustrate the geometric changes resulting from the shape optimization process. Upon examining the *xz*-plane with the highlighted region, it becomes evident that the original structure exhibits regular wave-like struts with consistent thickness in the *x*-direction, whereas the strut thickness in the *x*-direction is reduced after the shape optimization process, as depicted in Fig. 3. This geometric alteration is observed in all three structures. The reason for this lies in the fact that the transverse struts in the *x*-direction are minimally stressed at these points due to the specified deformation, resulting in a reduction in volume.

Furthermore, it is noteworthy that manufacturing the optimized structures posed a challenge at times, as the walls of the shape-optimized gyroid structures became very thin and fragile in certain areas due to the optimization process. Therefore, a loss of accuracy in replicating the digital structures by 3D printing is introduced.

4.2.2 Mechanical testing condition

The experimental validation of the unidirectional shape-optimized gyroidal unit cells based on the phase-field method is conducted according to the ASTM D1621 standard, "Standard Test Method for Compressive Properties of Rigid Cellular Plastics" [57]. Accordingly, the sizing of the samples, as well as the testing conditions and evaluations, are based on the standard. For conducting the compression tests, the *inspekt 200* machine from *Hegewald & Peschke* is utilized. The testing is initiated with compression at a pressure of 0.03 kPa and is conducted at a testing speed of 2.95 mm/min. The test is terminated upon reaching approximately 13 % of the original thickness. For subsequent evaluations, the values are zeroed from a force load of 10 N.

4.2.3 Experimental validation of the phase-field simulation results of shape optimization

In comparison to homogeneous materials, local stress peaks are more pronounced in porous structures leading to a relatively small range of linear elastic behaviour due to local plastification being established at relatively small macroscopic strains. This can also be seen from the stress–strain diagram in Fig. 11 of the three considered structure types. In the stress–strain diagram, the average measurement curves with their respective standard deviations are depicted. The dashed blue lines refer to the initial structures (I), while the solid green lines represent the shape-optimized (O) structures.

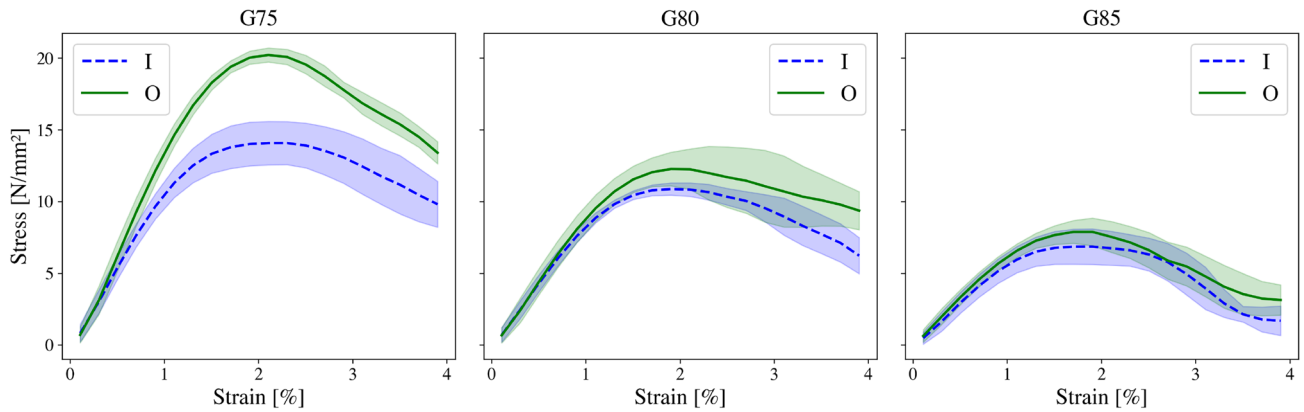

Fig. 11 Stress–strain curve of averaged experimental data including standard deviation for the initial and optimized gyroid structures with porosities of 75 % (G75), 80 % (G80), and 85 % (G85)

Table 3 Comparison of the effective modulus of elasticity from the experiments (mean: $\bar{E}$, standard deviation: $\widetilde{E}$) and simulations (dimensionalized: $\bar{E}_{\text{Sim}}$)

		G75		G80		G85	
		Initial	Optimized	Initial	Optimized	Initial	Pptimized
$\bar{E}$	[MPa]	70.726	99.511	59.107	64.026	42.327	46.200
$\widetilde{E}$	[MPa]	11.426	2.750	3.133	6.589	3.980	2.533
$\bar{E}_{\text{Sim}}$	[MPa]	69.395	101.974	50.672	70.995	39.773	53.427

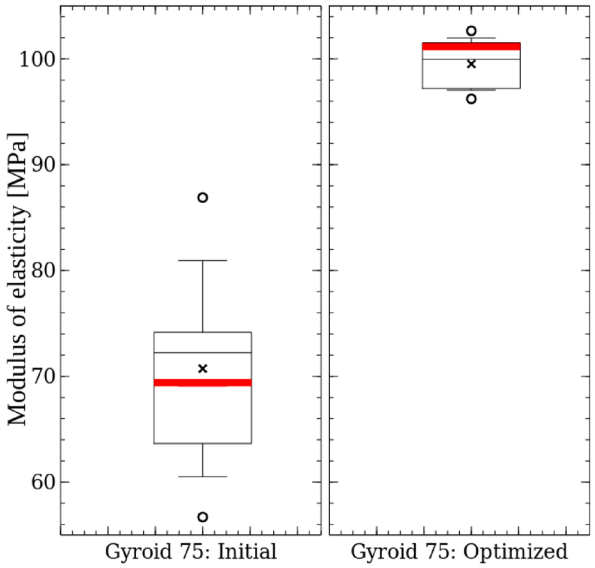

Fig. 12 Comparison of simulated and experimentally determined elastic moduli from compression tests of the gyroid structure with a volume fraction of 0.25 [-]. The solid red bar represents the dimensionalised Young's modulus obtained from simulation, while the cross denotes the mean of the experimentally obtained data. Whiskers indicate the standard deviation, and outliers are marked by points

From the stress–strain diagram, it is evident that the average measurement curve of the optimized structures lies above the course of the initial sample types. This clearly shows that the shape optimization results in increased stiffness within the linear elastic regime. Furthermore, also in the plastic range improvements are observed compared to the original structures. Therefore, improvements from the elastic optimization can also be transferred to plastic properties. The gyroid structure with a volume fraction of 0.25 [-] (G75) records the highest load capacity, followed by the structure with a porosity of volume fraction of 0.20 [-] (G80) and 0.15 [-] (G85). The greatest optimization success is clearly achieved with the G75 structure. This is because the largest volume redistribution occurred in the structure with a porosity of 75 %. From the respective force-displacement diagrams, the Young's moduli for each individual sample are determined using the formula suggested in the ASTM D1621 standard. The modulus of elasticity (E) is calculated as

$$E = \frac{WH}{AD}, \tag{16}$$

where W [N] is the load, H [m] the height of the undeformed sample, A [m^2], the horizontal cross-sectional area, and D [m] denotes the deformation. For the determination of D and W, two localized areas of the sample from the linear-elastic range are selected. Since the guideline does not provide specific details about the choice of points, the local area of each sample where the strain is 0.1% is selected. To ensure a consistent determination of the W size, the respective values at which the strain is 30% of the difference between the strain at 0.1% and the strain at maximum stress are considered. As these are porous specimens, the horizontal cross-sectional area in A, [m^2], the area of the samples is treated as if it was a solid material. In Table 3 the average calculated effective Young's modulus from the experimental data $\bar{E}$, as well as their standard deviation $\widetilde{E}$, are listed. For a better overview and comparison between the experimental and simulation data, the dimensionless Young's moduli from Table 1 are dimensionalized and also listed ($\bar{E}_{\text{Sim}}$).

When examining the average Young's modulus, it is clear that the optimized structures all exhibit a higher Young's modulus compared to their original structures. The highest variations in the calculated Young's modulus are seen in the initial structures of 75 %, while its optimized counterpart with a deviation of 2.750 MPa shows a minor deviation.

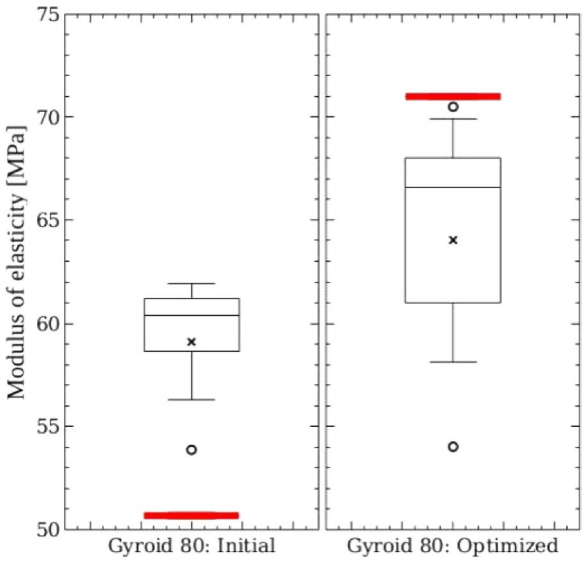

Fig. 13 Comparison of simulated and experimentally determined elastic moduli from compression tests of the gyroid structure with a volume fraction of 0.20 [-]. The solid red bar represents the dimensionalised Young's modulus obtained from simulation, while the cross denotes the mean of the experimentally obtained data. Whiskers indicate the standard deviation, and outliers are marked by points

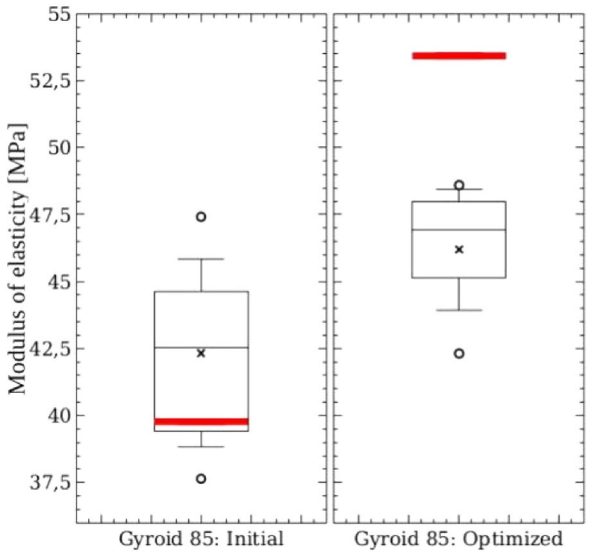

Fig. 14 Comparison of simulated and experimentally determined elastic moduli from compression tests of the gyroid structure with a volume fraction of 0.15 [-]. The solid red bar represents the dimensionalised Young's modulus obtained from simulation, while the cross denotes the mean of the experimentally obtained data. Whiskers indicate the standard deviation, and outliers are marked by points

On average, the effective Young's modulus could be increased by about 40 %. For the gyroid structure with a porosity of 80 %, the optimization process achieved an increase of 9.8 % and the structure with the highest porosity of 85 % achieved the smallest increase in the effective Young's modulus with an increase of 2.4 %. For further comparison, the values are illustrated in box plots in Figs. 12, 13,14. The red, thick bar symbolizes the dimensionalized Young's modulus. The cross marks the mean and the round dots denote the outliers of the respective sample series. Additionally, the whiskers indicate the standard deviation. When comparing the box plots between samples with different porosities, attention should be paid to the scaling of the *y*-axis.

When examining the box plots, it is noticeable that the experimental and simulation data of the gyroid structure with volume fraction of 0.25 [-] match the best, while the simulation data for the gyroid structures with volume fractions of 0.2 [-] and 0.15 [-] do not always fall within the experimentally determined data ranges. The highest deviation is observed in the samples with a volume fractions of 0.2 [-] and optimized structures with a volume fractions of 0.15 [-], with an average deviation of approximately 15 %. The samples with higher volume fraction (G75) show the smallest deviation from the simulation results, possibly due to challenging manufacturing quality caused by thin walls and small cell size. Nonetheless, the experimental validation confirmed that a load-specific optimization using the phase-field method while maintaining the periodicity of complex porous structures is successfully feasible. This confirmation not only opens up the possibility to optimize gyroid structures but also other complex structures.

Thanks to the successful maintenance of periodicity in all spatial directions during the optimization process, there is the option to optimize unit cells and then multiply them accordingly in the respective directions. This opens up a multitude of design possibilities for various industrial applications where stability and low weight are important.

5 Summary and outlook

Under the constraints of constant volume fraction and preserving periodicity of the structure, a modified phase-field method for the shape optimization process is applied to computationally determine shape optimized complex porous structures. During the shape optimization process, volume redistribution occurs by shifting the interface. In contrast to the conventional phase-field method, where the goal is to minimize energy, the objective is to maximize energy to achieve higher stiffness. It is demonstrated that shape optimization of complex porous structures while maintaining characteristic properties such as periodicity is feasible using a modified phase-field equation under both unidirectional and multidirectional loading conditions. For unidirectional loading, three gyroidal unit cells with volume fractions of 0.25 [-], 0.2 [-], and 0.15 [-] are shape optimized by increasing the strain energy to enhance stiffness while prescribing a macroscopic strain. It is observed that the effective modulus of elasticity increased for all three structures, while the surface area slightly decreased for structures with volume fractions of 0.2 [-] and 0.15 [-]. The surface area increased minimally for the 75 % porosity. The highest increase is achieved for the gyroid structure with a volume fraction of 0.25 [-], attributed to the greatest volume redistribution due to the lower porosity. In addition to unidirectional loading, various loading scenarios are examined in the multidirectional case, with the gyroidal unit cell with a volume fraction of 0.15 [-] subjected to both shear and compressive loading. Similar to the unidirectional case, an increase in the modulus of elasticity is achieved, while the surface area is reduced by approximately 2 %. After demonstrating the feasibility of load-specific phase-field-based shape optimization simulations, the unidirectionally loaded shape-optimized structures are experimentally validated. Experimental validation followed the ASTM D1621 standard. The evaluation of the test specimens shows that, on average, the shape-optimized structures exhibit higher stiffness in the respective loading directions. The optimization of the structures influence both the linear elastic and plastic range. As evident from the simulations, the optimized gyroid structure with a volume fraction of 0.25 [-] achieves an average increase in the effective modulus of elasticity of 40 %.

Overall, the load-specific shape optimization based on the phase-field approach offers promising prospects for various applications across different industries. By preserving key structural characteristics such as periodicity throughout the optimization process, complex structures can be tailored to specific loading scenarios. This capability holds immense potential for developing efficient and customized solutions in fields such as medical engineering.

A comprehensive analysis of phase-field-based topological optimization appears as a promising avenue to further leverage the capabilities of this method. By strategically altering the topology and subsequently optimizing the shape, there is the possibility to create new, innovative structures for application-specific loading conditions.

Acknowledgements A special thanks goes to Andreas Reiter for his time and discussions. Also, thanks to Prof. Dr.-Ing. Wasmuth and Mrs. Kirchlechner for conducting and supporting the experimental investigation. Gratitude is extended to the Federal Ministry of Economics and Climate Protection for their funding of the ZIM projects KK5134113SK1 and KK5446701SK1. Financial support for advancing the modelling and implementation by the Helmholtz association through the programme "MSE", no. 43.41.01, is gratefully acknowledged. This work was performed on the computational resource bwUniCluster funded by the Ministry of Science, Research and the Arts Baden-Württemberg and the Universities of the State of Baden-Württemberg, Germany, within the framework program bwHPC.

Funding Open Access funding enabled and organized by Projekt DEAL.

Data Availability The data that support the findings of this study are available upon reasonable request.

Details on the discretisation

Subsequently, details of the discretisation schemes employed in this work are given. The spatial discretization is based on an equidistant Cartesian grid. The subscripts *i*, *j*, *k* are used to index the grid cells, while the superscript *n* indicates the time step.

Phase-field evolution

Subsequently, the phase variable of the solid phase is abbreviated using $\phi := \phi_s$ and it is saved on the cell centers of the grid. For the phase-field evolution, the a first order explicit integration is employed yielding

$$\phi_{i,j,k}^{n+1} = \phi_{i,j,k}^{n} + \Delta t \Psi_{i,j,k}(\phi^n, \boldsymbol{u}^n) \tag{17}$$

with the time step width Δt and the incremental function Ψ which depends only on the phase-field and displacement field of the current time step *n*. it consists of the right hand side of equation (14) at time $t^n = n\Delta t$ and thus is given as

$$\Psi = \frac{M}{\epsilon}\left[2\gamma\epsilon(\Delta\phi - \|\nabla\phi\|\nabla\cdot\boldsymbol{n}) - \frac{16\gamma}{\pi^2\epsilon}(1-2\phi) - \lambda_{\text{vol}} + \frac{\partial h(\phi)}{\partial\phi}f_{\text{el}}\right]. \tag{18}$$

The increment function is discretized in space. While most terms therein are straight forward, the discretization of the curvature corrected Laplace term is subsequently discussed. Thereby, the identity

$$\Delta\phi - \|\nabla\phi\|\nabla\cdot\boldsymbol{n} = \nabla(\|\nabla\phi\|)\cdot\boldsymbol{n} \tag{19}$$

is exploited, which holds due to $\boldsymbol{n} = \nabla\phi/\|\nabla\phi\|$. The discretization of $\nabla(\|\nabla\phi\|)\cdot\boldsymbol{n}$ at cell center location requires the corresponding gradient, which is approximated using the central difference scheme

$$\nabla\phi(t^n, \boldsymbol{x}_{i,j,k}) \approx \left[\frac{\phi_{i+1,j,k}^n - \phi_{i-1,j,k}^n}{2\Delta x}, \frac{\phi_{i,j+1,k}^n - \phi_{i,j-1,k}^n}{2\Delta y}, \frac{\phi_{i,j,k+1}^n - \phi_{i,j,k-1}^n}{2\Delta z}\right]^\top. \tag{20}$$

The other factor, which needs to be discretized is ∇g with $g := \|\nabla\phi\|$. This is calculated with central differences using the values of *g* at the cell faces and thus

$$\nabla g \approx \left[\frac{g_{i+1/2,j,k}^n - g_{i-1/2,j,k}^n}{\Delta x}, \frac{g_{i,j+1/2,k}^n - g_{i,j-1/2,k}^n}{\Delta y}, \frac{g_{i,j,k+1/2}^n - g_{i,j,k-1/2}^n}{\Delta z}\right]^\top. \tag{21}$$

The discretisation scheme to obtain these face center values is exemplarily given for $g_{i+1/2,j,k}^n$, which is calculated using the norm of

$$\nabla\phi(t^n, \boldsymbol{x}_{i+1/2,j,k}) \approx \begin{bmatrix} \frac{\phi_{i+1,j,k}^n - \phi_{i,j,k}^n}{\Delta x} \\ \frac{1}{4\Delta y}(\phi_{i,j+1,k}^n + \phi_{i+1,j+1,k}^n) - (\phi_{i,j-1,k}^n + \phi_{i+1,j-1,k}^n) \\ \frac{1}{4\Delta y}(\phi_{i,j,k+1}^n + \phi_{i+1,j,k+1}^n) - (\phi_{i,j,k-1}^n + \phi_{i+1,j,k-1}^n) \end{bmatrix}. \tag{22}$$

For the transversal components, this is corresponds to the linear interpolation of a central difference with respect to the cell centers of both cells adjacent to the face. The other values are obtained by a similar scheme.

Mechanical equilibrium

The stationary momentum balance $\nabla\cdot\boldsymbol{\sigma} = \boldsymbol{0}$ is solved every time step *n* (cf. Fig. 2) using a linear finite element discretization. The displacement field serves as solution variable and is stored at the grid nodes, while stress and strain are stored at the cell centers. A reduced integration is used and thus the effective stiffness for integration over an element can be directly obtained by $\phi_{i,j,k}\mathbb{C}$ using the cell center values of ϕ.

References

1. Ingrole A, Aguirre TG, Fuller L, Donahue SW. Bioinspired energy absorbing material designs using additive manufacturing. J Mech Behav Biomed Mater. 2021;119: 104518. https://doi.org/10.1016/j.jmbbm.2021.104518.
2. Vincent J, Bogatyreva O, Bogatyrev N, Bowyer A, Pahl A-K. Biomimetics: its practice and theory. J R Soc. 2006;3:471–82. https://doi.org/10.1098/rsif.2006.0127.
3. Zhang Q, Yang X, Li P, Huang G, Feng S, Shen C, Han B, Zhang X, Jin F, Xu F, Lu TJ. Bioinspired engineering of honeycomb structure - using nature to inspire human innovation. Progress in Materials Science 2015;74, 332–400 https://doi.org/10.1016/j.pmatsci.2015.05.001
4. Ataee A, Li Y, Fraser D, Song G, Wen C. Anisotropic ti-6al-4v gyroid scaffolds manufactured by electron beam melting (ebm) for bone implant applications. Mater Des. 2018;137:345–54. https://doi.org/10.1016/j.matdes.2017.10.040.
5. Maharjan GK, Khan SZ, Riza SH, Masood S. Compressive behaviour of 3d printed polymeric gyroid cellular lattice structure. IOP Conference Series: Materials Science and Engineering. 2018;455(1): 012047. https://doi.org/10.1088/1757-899X/455/1/012047.
6. Cooke MN, Fisher JP, Dean D, Rimnac C, Mikos AG. Use of stereolithography to manufacture critical-sized 3d biodegradable scaffolds for bone ingrowth. J Biomed Mater Res B. 2003;64B(2):65–9. https://doi.org/10.1002/jbm.b.10485.
7. Olsson A, Hellsing MS, Rennie AR. New possibilities using additive manufacturing with materials that are difficult to process and with complex structures. Physica Scripta. 2017;92(5): 053002. https://doi.org/10.1088/1402-4896/aa694e.
8. Ashby M. The properties of foams and lattices. Philosophical transactions. Series A, Mathematical, physical, and engineering sciences 2005;364, 15–30 https://doi.org/10.1098/rsta.2005.1678
9. Kechagias S, Oosterbeek RN, Munford MJ, Ghouse S, Jeffers JRT. Controlling the mechanical behaviour of stochastic lattice structures: the key role of nodal connectivity. Add Manuf. 2022;54: 102730. https://doi.org/10.1016/j.addma.2022.102730.
10. Siegkas P, Tagarielli V, Petrinic N. Modelling stochastic foam geometries for fe simulations using 3d voronoi cells. Procedia Materials Science 2014;4, 221–226 https://doi.org/10.1016/j.mspro.2014.07.604 . 8th International Conference on Porous Metals and Metallic Foams
11. Hsieh M-T, Endo B, Zhang Y, Bauer J, Valdevit L. The mechanical response of cellular materials with spinodal topologies. J Mech Phys Solids. 2019;125:401–19. https://doi.org/10.1016/j.jmps.2019.01.002.
12. Torres-Sanchez C, Borgman J, Sargeant B, Bell H, Alabort E, Lindsay C, Conway P. Comparison of slm cpti sheet-tpms and trabecular-like strut-based scaffolds for tissue engineering. Adv Eng Mater. 2021. https://doi.org/10.1002/adem.202100527.
13. Maevskaia E, Guerrero J, Ghayor C, Bhattacharya I, Weber FE. Triply periodic minimal surface-based scaffolds for bone tissue engineering: A mechanical, in vitro and in vivo study. Tissue Eng A. 2023;29(19–20):507–17. https://doi.org/10.1089/ten.tea.2023.0033. (**PMID: 37212290**).
14. Hesselmann F, Scherenberg N, Bongartz P, Djeljadini S, Wessling M, Cornelissen C, Schmitz-Rode T, Steinseifer U, Jansen SV, Arens J. Structure-dependent gas transfer performance of 3d-membranes for artificial membrane lungs. J Membr Sci. 2021;634: 119371. https://doi.org/10.1016/j.memsci.2021.119371.
15. Dixit T, Al-Hajri E, Paul MC, Nithiarasu P, Kumar S. High performance, microarchitected, compact heat exchanger enabled by 3d printing. Appl Therm Eng. 2022;210: 118339. https://doi.org/10.1016/j.applthermaleng.2022.118339.
16. Gado MG, Al-Ketan O, Aziz M, Al-Rub RA, Ookawara S. Triply periodic minimal surface structures: Design, fabrication, 3d printing techniques, state-of-the-art studies, and prospective thermal applications for efficient energy utilization. Energy Technology n/a(n/a), 2301287 doi: 10.1002/ente.202301287 https://onlinelibrary.wiley.com/doi/pdf/10.1002/ente.202301287
17. Zargham S, Ward T, Ramli R, Badruddin I. Topology optimization: a review for structural designs under vibration problems. Struct Multidisc Optim. 2016. https://doi.org/10.1007/s00158-015-1370-5.
18. Schumacher A. Optimierung Mechanischer Strukturen: Grundlagen und Industrielle Anwendungen. 2020. https://doi.org/10.1007/978-3-662-60328-4.
19. Ansola R, Canales J, TÃ¡rrago JA, Rasmussen J. An integrated approach for shape and topology optimization of shell structures. Computers & Structures 2002;80(5), 449–458 https://doi.org/10.1016/S0045-7949(02)00019-6
20. Gibson LJ. Cellular solids. MRS Bull. 2003;28(4):270–4. https://doi.org/10.1557/mrs2003.79.
21. Germain L, Fuentes CA, Vuure AW, des Rieux A, Dupont-Gillain C. 3d-printed biodegradable gyroid scaffolds for tissue engineering applications. Mater Des 2018;151, 113–122 https://doi.org/10.1016/j.matdes.2018.04.037
22. Kanwar S, Vijayavenkataraman S. 3d printable bone-mimicking functionally gradient stochastic scaffolds for tissue engineering and bone implant applications. Mater Design. 2022;223: 111199. https://doi.org/10.1016/j.matdes.2022.111199.
23. Liu S, Feng J, Zhang F, Jiang W, Vasilieva TM, Lu P, Lu S. Parametric design and performance study of continuous gradient triply periodic minimal surface bone scaffold. IJB 2024;0(0), 2306 https://doi.org/10.36922/ijb.2306
24. Wallat L, Altschuh P, Reder M, Nestler B, Poehler F. Computational design and characterisation of gyroid structures with different gradient functions for porosity adjustment. Materials. 2022;15:10. https://doi.org/10.3390/ma15103730.
25. Wallat L, Selzer M, Wasmuth U, Poehler F, Nestler B. Energy absorption capability of graded and non-graded sheet-based gyroid structures fabricated by microcast processing. J Mater Res Technol. 2022;21:1798–810. https://doi.org/10.1016/j.jmrt.2022.09.093.
26. Günther F, Pilz S, Hirsch F, Wagner M, Kästner M, Gebert A, Zimmermann M. Shape optimization of additively manufactured lattices based on triply periodic minimal surfaces. Add Manuf. 2023;73: 103659. https://doi.org/10.1016/j.addma.2023.103659.
27. Wallat L, Reder M, Selzer M, Poehler F, Nestler B. Shape optimization of porous structures by phase-field modeling with strain energy density reduction. Mater Today Commun. 2023;37: 107018. https://doi.org/10.1016/j.mtcomm.2023.107018.
28. Bendsøe MP. Optimization of Structural Topology, Shape, and Material, vol. 414. Berlin; Heidelberg: Springer; 1995.
29. Li X, Lowengrub J, Rätz A, Voigt A. Solving pdes in complex geometries: a diffuse domain approach. Commun Math Sci. 2009;7(1):81–107. https://doi.org/10.4310/cms.2009.v7.n1.a4.
30. Takezawa A, Koizumi Y, Kobashi M. High-stiffness and strength porous maraging steel via topology optimization and selective laser melting. Add Manuf. 2017;18:194–202. https://doi.org/10.1016/j.addma.2017.10.004.

31. Blank L, Garcke H, Sarbu L, Srisupattarawanit T, Styles V, Voigt A. In: Leugering, G., Engell, S., Griewank, A., Hinze, M., Rannacher, R., Schulz, V., Ulbrich, M., Ulbrich, S. (eds.) Phase-field Approaches to Structural Topology Optimization, pp. 245–256. Springer, Basel 2012. https://doi.org/10.1007/978-3-0348-0133-1_13 .
32. Wallin M, Ristinmaa M. Howard's algorithm in a phase-field topology optimization approach. Int J Num Meth Eng. 2013;94(1):43–59. https://doi.org/10.1002/nme.4434.
33. Auricchio F, Bonetti E, Carraturo M, Hömberg D, Reali A, Rocca E. A phase-field-based graded-material topology optimization with stress constraint. Math Models Methods Appl Sci. 2020;30(08):1461–83. https://doi.org/10.1142/S0218202520500281.
34. Xie W, Xia Q, Yu Q, Li Y. An effective phase field method for topology optimization without the curvature effects. Comput Math Appl. 2023;146:200–12. https://doi.org/10.1016/j.camwa.2023.06.037.
35. Takezawa A, Yonekura K, Koizumi Y, Zhang X, Kitamura M. Isotropic ti-6al-4v lattice via topology optimization and electron-beam melting. Add Manuf. 2018;22:634–42. https://doi.org/10.1016/j.addma.2018.06.008.
36. Wallat L, Koeppe A, Selzer M, Seiler M, Poehler F, Nestler B. Experimental evaluation of phase-field-based load-specific shape optimization of nature-inspired porous structures. Mater Today Commun. 2024;38: 108088. https://doi.org/10.1016/j.mtcomm.2024.108088.
37. Feng J, Liu B, Lin Z, Fu J. Isotropic porous structure design methods based on triply periodic minimal surfaces. Mater Design. 2021;210: 110050. https://doi.org/10.1016/j.matdes.2021.110050.
38. Feng J, Fu J, Yao X, He Y. Triply periodic minimal surface (tpms) porous structures: from multi-scale design, precise additive manufacturing to multidisciplinary applications. Int J Extr Manuf. 2022;4(2): 022001. https://doi.org/10.1088/2631-7990/ac5be6.
39. Michielsen K, Stavenga D. Gyroid cuticular structures in butterfly wing scales: Biological photonic crystals. J R Soc. 2007;5:85–94. https://doi.org/10.1098/rsif.2007.1065.
40. Hill R. On constitutive macro-variables for heterogeneous solids at finite strain. Proc R Soc Lond. 1972;326(1565):131–47.
41. Reder M, Holland-Cunz J, Lorson P, August A, Nestler B. Simulative determination of effective mechanical properties for digitally generated foam geometries. Adv Eng Mater. 2023;25(19):2300340. https://doi.org/10.1002/adem.202300340.
42. Nestler B, Choudhury A. Phase-field modeling of multi-component systems. Current Opinion in Solid State and Materials Science 2011;15(3), 93–105. Applications of Phase Field Modeling in Materials Science and Engineering
43. Wheeler AA, Boettinger WJ, McFadden GB. Phase-field model for isothermal phase transitions in binary alloys. Phys Rev A. 1992;45(10):7424.
44. Schoof E, Schneider D, Streichhan N, Mittnacht T, Selzer M, Nestler B. Multiphase-field modeling of martensitic phase transformation in a dual-phase microstructure. Int J Solids Struct. 2018;134:181–94. https://doi.org/10.1016/j.ijsolstr.2017.10.032.
45. Schneider D, Schwab F, Schoof E, Reiter A, Herrmann C, Selzer M, Böhlke T, Nestler B. On the stress calculation within phase-field approaches: a model for finite deformations. Comput Mech. 2017;60(2):203–17. https://doi.org/10.1007/s00466-017-1401-8.
46. Nestler B, Garcke H, Stinner B. Multicomponent alloy solidification: phase-field modeling and simulations. Phys Rev E. 2005;71: 041609. https://doi.org/10.1103/PhysRevE.71.041609.
47. Garcke H, Nestler B, Stoth B. A multiphase field concept: numerical simulations of moving phase boundaries and multiple junctions. SIAM J Appl Math. 1999;60(1):295–315. https://doi.org/10.1137/S0036139998334895.
48. Daubner S, Hoffrogge PW, Minar M, Nestler B. Triple junction benchmark for multiphase-field and multi-order parameter models. Comput Mater Sci. 2023;219: 111995. https://doi.org/10.1016/j.commatsci.2022.111995.
49. Prahs A, Reder M, Schneider D, Nestler B. Thermomechanically coupled theory in the context of the multiphase-field method. Int J Mech Sci. 2023;257: 108484. https://doi.org/10.1016/j.ijmecsci.2023.108484.
50. Allen SM, Cahn JW. A microscopic theory for antiphase boundary motion and its application to antiphase domain coarsening. Acta Metallurgica. 1979;27(6):1085–95. https://doi.org/10.1016/0001-6160(79)90196-2.
51. Nestler B, Wendler F, Selzer M, Stinner B, Garcke H. Phase-field model for multiphase systems with preserved volume fractions. Phys Rev E. 2008;78: 011604. https://doi.org/10.1103/PhysRevE.78.011604.
52. Khachaturyan AG. Theory of structural transformations in solids. New York: John Wiley and Sons; 1983.
53. Hoffrogge P, Mukherjee A, Nani E, Amos PK, Wang F, Schneider D, Nestler B. Multiphase-field model for surface diffusion and attachment kinetics in the grand-potential framework. Phys Rev E. 2021;103(3): 033307. https://doi.org/10.1103/PhysRevE.103.033307.
54. Sun Y, Beckermann C. Sharp interface tracking using the phase-field equation. J Comput Phys. 2007;220(2):626–53. https://doi.org/10.1016/j.jcp.2006.05.025.
55. Hötzer J, Reiter A, Hierl H, Steinmetz P, Selzer M, Nestler B. The parallel multi-physics phase-field framework pace3d. J Comput Sci. 2018;26:1–12. https://doi.org/10.1016/j.jocs.2018.02.011.
56. Qiu N, Zhang J, Li C, Shen Y, Fang J. Mechanical properties of three-dimensional functionally graded triply periodic minimum surface structures. Int J Mech Sci. 2023;246: 108118. https://doi.org/10.1016/j.ijmecsci.2023.108118.
57. Standard Test Method for Compressive Properties Of Rigid Cellular Plastics (2000)